

# Aberrant Neural Activity in Prefrontal Pyramidal Neurons Lacking TDP-43 Precedes Neuron loss

**Bo Liang**

University of North Dakota

**Rashmi Thapa**

University of Wyoming

**Gracie Zhang**

Laramie High School

**Casey Moffitt**

National Institute on Drug Abuse

**Yan Zhang**

National Institute on Drug Abuse

**Lifeng Zhang**

National Institute on Drug Abuse

**Amanda Johnston**

University of Wyoming

**Hyrum P. Ruby**

University of Wyoming

**Giovanni Barbera**

National Institute on Drug Abuse

**Philip C. Wong**

Johns Hopkins University School of Medicine

**Zhaojie Zhang**

University of Wyoming

**Da-Ting Lin**

National Institute on Drug Abuse

**Yun Li** (✉ [yli30@uwyo.edu](mailto:yli30@uwyo.edu))

University of Wyoming <https://orcid.org/0000-0002-5251-747X>

---

**Research article**

**Keywords:**

**Posted Date:** January 17th, 2022

**DOI:** <https://doi.org/10.21203/rs.3.rs-1215072/v1>

**License:**  This work is licensed under a Creative Commons Attribution 4.0 International License.

[Read Full License](#)

---

# Abstract

## Background:

Mislocalization of TAR DNA binding protein 43 kDa (TAPDBP, or TDP-43) is a principle pathological hallmark identified in cases of neurodegenerative disorders such as amyotrophic lateral sclerosis (ALS) and frontotemporal dementia (FTD). As an RNA binding protein, TDP-43 serves in the nuclear compartment to repress nonconserved cryptic exons to ensure the generation of a normal transcriptome. Since nuclear depletion of TDP-43 is frequently observed independent of its cytosolic accumulation, a loss-of-function mechanism has been proposed to contribute to neurodegeneration. Multiple lines of evidence from animal models and human studies support the view that loss of TDP-43 leads to neuron loss, independent of its cytosolic aggregation. However, the underlying pathogenic pathways driven by the loss-of-function mechanism are still poorly defined.

## Methods:

We employed a genetic approach to determine the impact of TDP-43 loss in pyramidal neurons of the prefrontal cortex (PFC). Young adult male homozygous floxed *Tdp-43<sup>F/F</sup>* mice were bilaterally injected into the PFC with mixed viruses containing a Cre virus driven by the CaMKII promoter and a Cre-dependent virus expressing a genetically encoded green fluorescent calcium indicator, GCaMP6f. This approach allowed us to specifically deplete TDP-43 and express GCaMP6f in pyramidal neurons of the PFC. We also bilaterally injected a virus expressing GCaMP6f driven by the CaMKII promoter into the PFC of age-matched male *Tdp-43<sup>F/F</sup>* mice as controls. Using a custom-built miniscope imaging system, we performed repetitive *in vivo* calcium imaging from freely behaving mice for up to 7 months, to monitor the dynamic changes of calcium activity in PFC pyramidal neurons of TDP-43 depleted and TDP-43 intact mice.

## Results:

By comparing calcium activity in PFC pyramidal neurons between TDP-43 depleted and TDP-43 intact mice, we demonstrated remarkably increased numbers of pyramidal neurons exhibiting hyperactive calcium activity after short-term TDP-43 depletion, followed by rapid activity declines during disease progression. We further demonstrated that long-term TDP-43 depletion was accompanied by a significant reduction in neuron numbers and increased gliosis in the PFC.

## Conclusions:

Our results suggest that TDP-43 loss-of-function drives dynamic changes in neural activity prior to neurodegeneration, highlighting the role of aberrant neural activity and dysfunctional calcium signaling in

the pathogenesis of neurodegenerative diseases including ALS and FTD.

## Background

TAR DNA-binding protein 43 kDa (TARDBP, or TDP-43) is a highly conserved nuclear DNA/RNA binding protein important for transcription regulation [1, 2]. Mislocalization of TDP-43, either abnormally accumulated into cytosolic or nuclear inclusions, is a common pathological feature of several neurodegenerative diseases, including amyotrophic lateral sclerosis (ALS), frontotemporal dementia (FTD), and Alzheimer's disease (AD) [3–5]. FTD and ALS sharing clinical, genetic, and pathological signatures, have been proposed to represent two extremes of one broad spectrum of neurodegenerative disorder [6]. Missense mutations in TDP-43 have been identified in familial and sporadic ALS cases [7, 8], as well as, in rare FTD cases [9, 10]. Most of these mutations are at the C-terminal region of TDP-43, which is important for interaction with members of heterogeneous nuclear ribonucleoproteins (hnRNPs) [11]. Association of TDP-43 genetic mutations with ALS and FTD supports the idea that TDP-43 is mechanistically linked to neurodegeneration. A gain-of-function mechanism due to TDP-43 cytoplasmic aggregates has been proposed to contribute to neurodegeneration [12, 13]. In addition, a loss-of-function mechanism caused by TDP-43 nuclear clearance has also been implicated in the pathogenesis process [14].

Several lines of evidence strongly support the loss-of-function mechanism as the major pathogenesis pathway towards neurodegeneration. First, studies from numerous TDP-43 knockdown and knockout models in worms, flies, fish and rodents [15–21], indicate that decrease or loss of TDP-43 expression leads to neuron loss [16, 18, 22, 23]. Second, no correlation has been established between the presence of cytoplasmic aggregates and neurodegeneration in transgenic mice expressing mutant forms of human TDP-43, where neurodegeneration occurs in motor neurons [24–26], as well as pyramidal neurons in the frontal cortex of several mouse lines [25, 26]. These observations indicate that cytoplasmic aggregates are not required to induce neurodegeneration [25, 27]. Third, clinical studies discover TDP-43 nuclear depletion occurs in brain neurons at a pre-symptomatic stage without cytoplasmic inclusions in some FTD cases [28, 29], supporting the notion that loss of TDP-43 represents an early event that drives neuron loss. Fourth, TDP-43 serves in the nuclear compartment to repress nonconserved cryptic exons during RNA splicing [30], and incorporation of nonconserved cryptic exons has been documented not only in brain transcriptomes of ALS and FTD cases [30], but also in AD cases exhibiting TDP-43 pathology [31]. Fifth, ALS-linked TDP-43 mutants from fibroblast-derived human motor neurons fail to repress nonconserved cryptic exons, independent of TDP-43 cytoplasmic aggregates [32, 33]. Finally, TDP-43 also represses a cryptic exon splicing in *UNC13A*, a top genetic allele to increase risk for ALS and FTD [34, 35].

All these observations highlight the need to understand the pathogenic mechanism by which TDP-43 loss-of-function drives neurodegeneration independent of its toxic gain-of-function from cytosolic inclusions. As a nuclear DNA/RNA binding protein, TDP-43 binds to UG-rich regions to regulate RNA processing, including mRNA splicing [1, 2, 30]. Although genome-wide analyses have identified a large number of genes and transcripts regulated by TDP-43 [1, 2], the disease-relevant pathways are still poorly

defined. Emerging evidence suggests that neurodegeneration is related to progressive changes in individual neural activity and brain microcircuits. Aberrant neural activity and dysregulated calcium signaling have been documented in some mouse models of neurodegenerative diseases [36–41]. It is not clear whether TDP-43 loss-of-function mechanism drives aberrant neural activity prior to neuron loss.

We employed a genetic approach to determine the impact of TDP-43 loss on neural activity of pyramidal neurons from a mouse model. Several conditional TDP-43 knockout mouse lines have been developed to bypass embryonic lethality [15, 18, 19], since TDP-43 is essential for early embryogenesis [42, 43]. Among them, *Tdp-43<sup>F/F</sup>* mice is a mouse line in which the exon 3 of the mouse *Tdp-43* gene is flanked with two loxP sites [15]. In the presence of Cre recombinase, the TDP-43 coding sequence is disrupted and a stop codon is introduced prematurely. It was predicted that the truncated N-terminal TDP-43 fragment is nonfunctional, since it lacked the critical RNA-binding domain encoded by the exon 3 and the highly conserved C-terminal domain. It was later confirmed that even the predicted N-terminal TDP-43 fragment was not expressed upon Cre recombination [15]. To explore whether TDP-43 loss-of-function mediated neurodegeneration is related to aberrant calcium signaling in the cortical network, we measured calcium activity in pyramidal neurons of the prefrontal cortex from awake behaving *Tdp-43<sup>F/F</sup>* mice, and compared calcium activity between TDP-43 depleted and control mice. We found that TDP-43 deletion induced aberrant neuronal activity changes, initially hyperactivity followed by a rapid activity decline, prior to neuron loss. These data implicate early dysfunctions in intracellular calcium signaling as a convergent point that may ultimately lead to neurodegeneration.

## Materials And Methods

### Animals

All experimental procedures were approved by the Institutional Animal Care and Use Committee of the University of Wyoming and the National Institute on Drug Abuse (NIDA), and were conducted in accordance with the guidelines of the National Institutes of Health. *Tardbp flox/flox* (loxP sites flank exon 3 of *Tardbp*) male and female breeders were obtained from Dr. Philip Wong's laboratory at the Johns Hopkins University School of Medicine. This mouse line was bred and maintained at the NIDA and the University of Wyoming. Mice were housed up to five mice per cage under a 12 h light/dark cycle and given *ad libitum* access to food and water.

### Stereotaxic injection

18 male *Tardbp flox/flox* homozygous mice (*Tdp-43<sup>F/F</sup>*) aged 3–5 months weighing 25–35 grams were used for experiments, including 8 control mice and 10 knockout (KO) mice. Stereotaxic viral injection was performed bilaterally at the prelimbic region based on the published lab protocols [44, 45]. Mice were briefly anesthetized with 5% isoflurane in oxygen. The head was shaved and held on a stereotaxic stage with a heating pad at 35°C. Anesthesia was maintained with 1.5% isoflurane in oxygen throughout the surgery. An incision was made along the sagittal midline to expose the bregma and lambda. A 0.6 mm

dental burr was used to drill a small hole through the skull at the coordinates A/P: +1.94 mm and M/L: 0.5 mm on both hemispheres. For KO mice, bilateral injection of a viral mixture was performed, containing AAV1-CaMKII-Cre ( $1.2 \times 10^{13}$  GC/mL) and a Cre dependent AAV1-CAG-FLEX-GCaMP6f ( $1.3 \times 10^{13}$  GC/mL) in a ratio of 1:1. For control mice, AAV1-CaMKII-GCaMP6f ( $2.8 \times 10^{13}$  GC/mL) was diluted with saline in a ratio of 1:1. Through a microliter syringe controlled by a micro-pump, 500 nL of virus was infused into each side of the designated brain region (A/P: +1.94 mm, M/L: 0.5 mm, D/V: 1.75 mm) at a rate of 50 nL/minute. The virus was allowed to diffuse away for additional 5–10 minutes before the skull skin was stitched for closure. Mice were allowed to recover for 14 days before proceeding to the next step.

## Gradient-index (GRIN) lens implantation

GRIN lens implantation into the mouse dorsal prelimbic cortex was performed according to the previously described lab protocols [44, 45]. Mice were anesthetized with an intraperitoneal injection of Ketamine/Xylazine (Ketamine: 100 mg/kg; Xylazine: 15 mg/kg) initially and maintained with additional doses of Ketamine (50 mg/kg) during the surgery. Craniotomy was performed at the coordinates A/P 1.94 mm and M/L 0.8 mm on the right side using a 1.2 mm drill burr. The brain tissue was aspirated layer-by-layer to the depth of 1.8 mm (measured from the bregma), with a blunt-end 27-G needle that was connected to an in-house vacuum system. The needle holder was connected to a robotic arm inclined to a 10° angle laterally, and was controlled by a custom-built software (<https://github.com/liang-bo/AutoStereota>) [46]. During the entire aspiration process, the exposed brain tissue was continuously rinsed with the artificial cerebrospinal fluid (ACSF) containing 124 mM of NaCl, 2.5 mM of KCl, 1.25 mM of  $\text{NaH}_2\text{PO}_4$ , 1.2 mM of  $\text{MgCl}_2$ , 25 mM of glucose, 26 mM of  $\text{NaHCO}_3$  and 2.4 mM of  $\text{CaCl}_2$ . ACSF was bubbled with a gas mixture of 95%  $\text{O}_2$  and 5%  $\text{CO}_2$  and filtered through a 0.2  $\mu\text{m}$  filter. After the aspirated area was blood-free, a sterile GRIN lens (GRINTECH) was implanted into the well and secured with two layers of dental cement (first layer-Metabond, second layer-Duralay). The exposed GRIN lens was covered by a customized protection cap.

## Miniscope base mounting

All miniscopes used for the experiment were custom-built by Dr. Da-Ting Lin's group at NIDA IRP [47–49]. After 4 weeks of GRIN lens implantation, a miniscope base was permanently mounted on the mouse skull. For base mounting, a miniscope fitted with a base was brought closer to the GRIN lens with the help of a custom-built motorized controller to obtain the best focal plane and the base was then affixed to the skull using dental cement. The main body of the miniscope was detached from the base after the dental cement had hardened.

### In vivo calcium imaging during social behavior tests

Mice were briefly anesthetized with 5% isoflurane in oxygen and the miniscope was fastened onto the base. Mice were allowed to recover from isoflurane for at least 30 minutes in their home cages before performing the *in vivo* recordings.

Social behavior test was performed based on the previously published protocol [48]. The experiment was performed in an open square arena (42 cm x 42 cm x 30 cm) to facilitate calcium imaging where two small containers were placed near the two opposite corners (10 cm away from the sidewall of arena). The test was composed of two stages, “habituation (H)” and “sociability (SB)”, each 10-minute long. During H stage, the mouse was allowed to explore the two empty containers freely. In SB stage, an age and gender matched (male) stranger mouse (stranger 1) was placed inside one of the containers whereas the other container remained empty. SB stage measures the tendency of a subject mouse to spend more time exploring the container holding a social target compared to the empty container.

For recording, the mouse was brought closer to the behavior arena and the miniscope was connected to a cable linked with the data acquisition computer system. Simultaneous recordings of the calcium imaging and mouse behavior were collected in two different computers with the aid of a custom-built calcium image recording software (NeuView) and a behavior recording software (PointGrey FlyCap2). The behavior recording was triggered by NeuView so that both calcium and behavioral recordings were temporally synchronized frame by frame. The recordings were performed at a rate of 10 frames per second. Each 10-minute stage was broken down into two 5-minute recording sessions to prevent excessive heating of the miniscope. Repetitive *in vivo* calcium imaging was performed every 4–6 weeks for longitudinal study until no active neurons were identified through *in vivo* calcium imaging.

For behavior analysis, the mouse behavior was manually annotated frame by frame using a custom developed MATLAB program and the time spent by the subject mouse exploring the containers was calculated. It was considered that the subject mouse was exploring when it sniffed, bit, poked, or physically contacted the container.

## Calcium imaging data analysis

Calcium image processing: Calcium images were first registered using motion correction toolbox NoRMCorre [50]. Then a constrained non-negative matrix factorization (CNMF) based calcium image processing toolbox, CalmAn-MATLAB [51–53], was used to extract fluorescent calcium signals. We manually added additional seeds as necessary based on the correlation image calculated by the correlation of neighboring pixels of calcium images. Calcium traces ( $\Delta F/F$ ) and referred spikes were calculated using the functions of CalmAn toolbox. For each neuron, the amplitude of calcium traces was normalized to the maximum of  $\Delta F/F$  values, and then the average of normalized values over time were calculated (referred to as “area under curve”, or AUC). To calculate frequency, the spikes for each neuron were binarized with a threshold of 5 standard deviations, and then the averaged spike numbers per second were calculated.

Identification of hypoactive, intermediate, and hyperactive neurons (Figure 2 and 3): For each neuron, the averaged AUC per second during the H stage was calculated. A neuron was defined as hypoactive neuron if its averaged AUC value was less than 0.05 per second. A neuron was defined as hyperactive neuron if its averaged AUC value was greater than 0.5 per second. The rest of the neurons were defined as neurons with intermediate activity.

Data analysis for longitudinal *in vivo* imaging studies (Figure 4): *In vivo* calcium imaging recorded from all control and KO mice during five independent social behavior tests ranging from 75 to 300 days post viral injection were used for analysis. To monitor the dynamic changes in neuronal activity over time, the entire field of view (650  $\mu\text{m}$   $\times$  650  $\mu\text{m}$ ) from each mouse was divided into 10  $\times$  10 small sub-areas. Each sub-area (65  $\mu\text{m}$   $\times$  65  $\mu\text{m}$ ) typically contained 5–15 active neurons which were spatially closed to each other. AUC per second during the H stage was first calculated for each neuron. Subsequently, for each small sub-area, the regional AUC was calculated at each imaging time point using the averaged AUC from the group neurons within the small sub-area. Sub-areas containing less than 3 active neurons were excluded from the regional AUC calculation. Sub-areas with regional AUC values for less than three independent time points were also excluded from the analysis. To quantify the regional AUC changes over time, we collectively compared the regional AUC values from all sub-areas at three different time periods: 1) Early: 75 to 125 days post viral injection; 2) Intermediate: 150 to 200 days post viral injection; and 3) Late: 250 to 300 days post viral injection.

## **Brain tissue harvesting, immunostaining and confocal microscopy imaging**

After the completion of all *in vivo* calcium imaging, the control and KO mice were anesthetized with overdosed Ketamine/Xylazine (Ketamine: 250 mg/kg; Xylazine: 37.5 mg/kg) and perfused with 20 ml of phosphate-buffered saline (PBS) followed by 20 ml of 4% paraformaldehyde (PFA) in PBS. The brains were then post-fixed by 4% PFA in PBS overnight and stored in PBS at 4°C. The fixed mouse brains were sectioned using a vibratome (Leica VT1200S) and 60  $\mu\text{m}$  thick coronal sections were collected in 24-well plates containing PBS.

TDP-43 and NeuN immunostaining: To confirm TDP-43 knockdown and possible neuron loss, immunostaining was performed using anti-TDP43 and anti-NeuN antibodies. The free-floating brain slices were washed in PBS (3 times for 5 minutes each) and incubated in a blocking buffer containing 1% bovine serum albumin, 4% normal donkey serum and 0.3% Triton X-100 in PBS for 2 hours at room temperature. The slices were incubated with a primary antibody solution containing mouse monoclonal anti-NeuN antibody (1B7, Abcam, 1:1,000 diluted in blocking buffer) and rabbit polyclonal anti-TDP-43 antibody (10782-2-AP, Proteintech, 1:500 diluted in blocking buffer) overnight at 4°C. The slices were washed with PBS (5 times for 5 minutes each) and incubated with a secondary antibody solution containing 1:300 diluted Donkey anti-Mouse IgG conjugated with Cy5 (715-175-150, Jackson ImmunoResearch Laboratories) and 1:600 diluted Donkey anti-Rabbit IgG conjugated with Alexa Fluor 594 (711-585-152, Jackson ImmunoResearch Laboratories) for 2 hours at room temperature. After washing with PBS (5 times for 5 minutes each), the slices were mounted using antifading mounting medium with DAPI (Vector Laboratories) on slides for fluorescence imaging.

TDP-43 and Cre immunostaining: To estimate TDP-43 knockdown efficiency by AAV1-CaMKII-Cre virus, immunostaining was performed using anti-TDP43 and anti-Cre antibodies. 1:1000 diluted mouse monoclonal Cre antibody (MAB3120, Sigma-Aldrich) and 1:500 diluted rabbit polyclonal anti-TDP-43

antibody (10782-2-AP, Proteintech) in blocking buffer were used as primary antibodies. 1:300 diluted Donkey anti-Mouse IgG conjugated with Cy5 (715-175-150, Jackson ImmunoResearch Laboratories) and 1:600 diluted Donkey anti-Rabbit IgG conjugated with Alexa Fluor 594 (711-585-152, Jackson ImmunoResearch Laboratories) in blocking buffer were used as secondary antibodies.

Glial fibrillary acidic protein (GFAP) immunostaining: Immunostaining for GFAP was performed to stain the reactive astrocytes. 1:400 diluted rabbit anti-GFAP monoclonal antibody (MA5-33059, Invitrogen) was used as the primary antibody and 1:600 diluted Donkey anti-Rabbit IgG conjugated with Alexa Fluor 594 (711-585-152, Jackson ImmunoResearch Laboratories) as the secondary antibody. Density of GFAP positive cells for the control and KO groups were determined using QuPath (<https://qupath.github.io>) in the virus injected and non-injected regions.

Microglial and caspase immunostaining: 1:500 diluted mouse monoclonal caspase 3 antibody (sc-136219, Santa Cruz Biotechnology) and 1:300 diluted rabbit polyclonal Iba1 (10904-1-AP, Proteintech) in blocking buffer were used as primary antibodies. 1:300 diluted Donkey anti-Mouse IgG conjugated with Cy5 (715-175-150, Jackson ImmunoResearch Laboratories) and 1:600 diluted Donkey anti-Rabbit IgG conjugated with Alexa Fluor 594 (711-585-152, Jackson ImmunoResearch Laboratories) in blocking buffer were used as secondary antibodies.

Confocal imaging: Whole brain images were taken using a 2.5X objective to locate the prelimbic region and tile images of the prelimbic region were taken using a 20X objective using a laser scanning confocal microscope (ZEISS LSM 980). Excitation lasers of 405 nm, 488 nm, 561 nm, and 639 nm were used for DAPI, GCaMP6f, Alexa Fluor 594 and Cy5, respectively. The detection wavelengths used for DAPI, GCaMP6f, Alexa Fluor 594 and Cy5 were 410-499 nm, 511-590 nm, 596-652 nm and 652-750 nm, respectively.

## **Nissl staining and imaging**

Mouse brain sections were placed in gelatin-coated slides and allowed to dry overnight. The slides were washed in PBS (2 times, 5 minutes each) and rinsed in deionized water for 1 minute. The slides were dipped in 1:10 diluted cresyl violet (Abcam) solution in water at room temperature for 20 minutes. The slides were washed with double deionized water (2 times, 5 minutes each). The slides were then sequentially placed in 90% ethanol, 95% ethanol and two changes of 100% ethanol for 3 minutes each. The slides were finally dipped in 100% xylene (2 times, 3 minutes each). The sections were mounted in Permount mounting medium (Fisher Chemical) for imaging. Images were taken using a slide scanner (ZEISS Axio Scan Z.1) at 20X objective.

## **Quantification for immunostaining and Nissl staining**

To quantify TDP-43, NeuN, caspase-3 and Iba1 immunostaining, QuPath was used to measure the numbers of positively stained particles within the virus injected region (containing GCaMP6f signal) and non-injected region (no GCaMP6f signal), respectively. The ratios of particle density between the virus

injected and non-injected regions for TDP-43, NeuN, caspase-3 and Iba1 were determined and compared between the control and KO groups.

To quantify the TDP-43 knockdown efficiency by AAV1-CaMKII-Cre virus, QuPath was used to measure the numbers of Cre and TDP-43 positively stained particles within the virus injected region (containing GCaMP6f signal). The differences were calculated in percentage.

To quantify Nissl stained images, neuronal and glial count was determined using QuPath based on different sizes of nuclei. Nissl staining stains nuclei of both neurons and glia, but the neuronal and glial nuclei differ significantly in both shapes and size based on the Nissl staining [54]. After multiple trials, it was determined that the sizes of neuronal nuclei fall into 40–100  $\mu\text{m}^2$ , and the glial nuclei fall into 5–35  $\mu\text{m}^2$ . This parameter was used to differentiate neuronal and glial cells. Nuclei detection was set automatically and all counting was done blindly. The ratio of neuron or glial density in the virus injected and non-injected region was determined and compared between the control and KO groups.

## Statistical analysis

All values in the text and figure legends are represented as mean  $\pm$  SEM. Nonparametric statistics, Mann-Whitney test or Kolmogorov-Smirnov test were used for statistical analysis between two groups. Nonparametric statistics, Kruskal-Wallis test and Dunn's post hoc test, were used for statistical comparison among more than two groups of data. A p value less than 0.05 was considered statistically significant.

## Results

### TDP-43 deletion in excitatory neurons of the PFC initially leads to hyperactive calcium activity

We bilaterally injected adeno-associated viruses (AAVs) expressing Cre recombinase driven by the CaMKII promoter (AAV1-CaMKII-Cre) and a Cre-dependent GCaMP6f (a genetically encoded green fluorescent calcium indicator) in the medial prefrontal cortex (PFC) of young adult (i.e., 3–4 months old) *Tdp-43<sup>F/F</sup>* mice [15], to selectively delete TDP-43 and express GCaMP6f in pyramidal neurons in the PFC (Figure 1A, referred to as KO mice). In parallel, we injected AAV-CaMKII-GCaMP6f virus to the PFC of young adult *Tdp-43<sup>F/F</sup>* mice to express GCaMP6f in pyramidal neurons (Figure 1A, referred to as CTRL mice). Therefore, GCaMP6f labeled TDP-43 deleted pyramidal neurons in KO mice, whereas labeled TDP-43 intact pyramidal neurons in control (CTRL) mice. We then implanted a 1-mm diameter gradient index (GRIN) lens into the PFC of these KO and CTRL mice. *Via* a custom-built miniscope recording system [47–49], we performed *in vivo* calcium imaging during a 20-minute social behavior test containing two stages (10-minute each), namely, habituation (H) and sociability (SB). We found that KO mice exhibited normal sociability, like that of CTRL mice (Figure 1B).

We used a MATLAB calcium imaging process toolbox, CalmAn [51], to identify active neurons and extract fluorescence changes ( $\Delta F/F$ ) of GCaMP6f from cell bodies of these neurons as somatic calcium activity (**Supplementary Figure S1**). For each active neuron, the amplitude of calcium trace was normalized to the maximum of absolute  $\Delta F/F$  value. The frequency of spikes, as well as the average of normalized  $\Delta F/F$  values over time (referred to as “area under curve”, or AUC), were calculated and compared between CTRL and KO groups. We found that neurons in KO mice exhibited significant increases in spike frequency (Figure 1C) and AUC (Figure 1D) during each 10-minute stage, as well as, over the entire 20-minute recording (Kolmogorov-Smirnov test,  $p < 0.0001$ ). We next calculated the averaged calcium spike frequency and AUC from individual mice at each behavioral stage and found that the KO group exhibited significantly higher spike frequency and AUC than those of the CTRL group (spike frequency in CTRL and KO mice:  $0.048 \pm 0.003$  and  $0.056 \pm 0.002$  per second; AUC in CTRL and KO mice:  $0.205 \pm 0.020$  and  $0.242 \pm 0.015$  per second; Mann-Whitney test,  $p < 0.05$ , Figure 1E), indicating hyperactivity in PFC pyramidal neurons triggered by TDP-43 depletion.

### **Longitudinal *in vivo* calcium imaging reveals dynamic activity changes after TDP-43 deletion**

We then performed *in vivo* calcium imaging repetitively during the social behavior test every 4-6 weeks (Figure 2A). We successfully collected *in vivo* calcium imaging from four KO and four CTRL mice for up to 7 months (i.e., the first recording was performed 3 months after the viral injection, and the last recording was performed 10 months after the viral injection). We then compared the AUC of calcium traces during the H stage in PFC pyramidal neurons between KO and CTRL mice at the neuronal population level (Figure 2B). We showed that KO pyramidal neurons exhibited increased AUC activity 3 months after TDP-43 depletion, but reduced AUC activity 10 months after TDP-43 depletion compared to pyramidal neurons in CTRL mice (AUC activity from CTRL and KO at 3 months post-virus injection:  $0.205 \pm 0.006$  and  $0.269 \pm 0.009$  per second; CTRL and KO at 10 months post-virus injection:  $0.167 \pm 0.006$  and  $0.108 \pm 0.011$  per second; Kolmogorov-Smirnov test,  $p < 0.0001$ ).

Pyramidal neurons in the PFC display high heterogeneity in spontaneously occurring calcium transients [48]. We next compared the distribution of the average AUC of calcium traces from individual PFC pyramidal neurons between KO and CTRL mice at two time points: 3 months and 10 months post viral injection. We set the thresholds to define the intermediate range (0.05 to 0.5 per second) of AUC values. Neurons displaying AUC values outside of the intermediate range were referred to as either hypoactive or hyperactive neurons (Figure 2C, also see **Supplementary Figure S2**). Among pyramidal neurons from CTRL mice, while the majority displayed intermediate calcium activity, there were less than 10% of neurons displaying hyperactivity, and less than 20% of neurons displaying hypoactivity at both time points (top panels in Figure 2C and 2D). Interestingly, 3 months after TDP-43 depletion, there were two-fold increases in percentage of neurons displaying hyperactivity from the KO mice (16% in KO, bottom panel in Figure 2C) than that of CTRL mice (8% in CTRL, top panel in Figure 2C). By contrast, 10 months after TDP-43 depletion, there were almost three times as many hypoactive neurons observed in KO mice (54% in KO, bottom panel in Figure 2D) as that of CTRL mice (19% in CTRL, top panel in Figure 2D).

We also showed cell activity maps indicating hypoactive, intermediate, and hyperactive pyramidal neurons, from a representative KO mouse and a CTRL mouse at different time points following TDP-43 depletion (Figure 3). In both cases, the total detectable active neurons were slightly reduced with time probably due to the reduced viral expression of GCaMP6f. Nevertheless, the CTRL mouse exhibited a relatively stable activity pattern across different time points (e.g., similar proportion of hyperactive and hypoactive neurons over time). Importantly, the KO mouse exhibited substantially more hyperactive, but more hypoactive neurons, respectively, during early and later time following viral injection.

## Rapid activity decline associated with long term TDP-43 depletion

To monitor the dynamic changes in neuronal calcium activity during disease progression, an ideal approach is to follow individual neurons to monitor their dynamics over time. However, since intervals between our repetitive *in vivo* calcium imaging were 30–45 days, it was difficult to accurately identify the exact same neurons on cell maps recorded at different time points. As a practical substitute, we divided each imaged PFC brain region into multiple small sub-areas (size: 65  $\mu\text{m}$  by 65  $\mu\text{m}$ ) where a small group (typically 5–15) of spatially adjacent neurons can be identified (Figure 4A). We selected those sub-areas containing at least 3 neurons to measure their averaged AUC activity and followed their activity changes over time. Starting with 175 and 285 such small sub-areas in 8 CTRL mice and 10 KO mice, respectively, we plotted the time course of activity changes from the same sub-areas across disease progression (Figure 4B). We found that most CTRL mice displayed relatively stable activity over the time course of 7 months, whereas most KO mice displayed rapid activity declines over time. We further quantified the averaged AUC from all these small sub-areas during disease progression at three time periods: 80–100 days, 150–200 days, and 250–300 days post viral injection, referred to as early, intermediate and late stages (Figure 4C). We confirmed that the CTRL group displayed a constant AUC activity across time ( $0.177 \pm 0.008$ ,  $0.185 \pm 0.007$ ,  $0.214 \pm 0.022$ ; Kruskal-Wallis test,  $p = 0.50$ ), while the KO group showed dynamic activity changes, a rapidly reduced AUC activity following the initial hyperactivity ( $0.248 \pm 0.011$ ,  $0.155 \pm 0.017$ ,  $0.182 \pm 0.016$ ; Kruskal-Wallis test,  $p < 0.0001$ ; Dunn's post hoc test, early vs intermediate,  $p < 0.0001$ ). These data suggest that long term depletion of TDP-43 in the PFC causes a rapid activity decline in pyramidal neurons.

## Immunohistochemistry analysis reveals neuron loss and gliosis

We harvested brain tissues after the very last *in vivo* calcium imaging and performed a series of immunohistochemistry studies (Figure 5). We first confirmed TDP-43 depletion in the KO brain tissues and demonstrated that the knockout efficiency of the AAV-CaMKII-Cre virus was 86.96% (**Supplementary Figure S3**). We further demonstrated that TDP-43 depletion was accompanied by a significant reduction in NeuN staining (Figure 5A). We then performed Nissl stain and compared neuronal and glial cell densities between CTRL and KO groups. In Nissl stained sections, neurons can be distinguished from glial cells by their different staining patterns and sizes. Neurons typically display larger stained nuclei and

lightly stained proximal segments of dendritic processes, while glial cells contain less stained endoplasmic reticulum and smaller nuclei [54]. Therefore, the parameters for glial and neuronal nuclei were set as 5–35  $\mu\text{m}^2$  and 40–100  $\mu\text{m}^2$ , respectively. Nuclei detection was performed automatically, and neuronal and glial counting was done blindly across all brain sections. The ratios of neuronal and glial density at the virus injected and non-injected areas were determined and compared between the CTRL and KO groups. Within the virus injected areas of KO mice, there were significantly reduced neurons (ratios in CTRL and KO:  $1.16 \pm 0.06$  and  $0.92 \pm 0.05$ , Mann-Whitney test,  $p < 0.01$ ), yet significantly increased glial cells (ratios in CTRL and KO:  $1.11 \pm 0.05$  and  $1.31 \pm 0.06$ , Mann-Whitney test,  $p < 0.05$ ) than those of CTRL mice (Figure 5B). GFAP staining further revealed that virus injected areas in KO mice exhibited substantially more GFAP signals than that of CTRL mice (non-injected and virus injected CTRL:  $21.4 \pm 5.9$  and  $100.0 \pm 34.8$ ; non-injected and virus injected KO:  $89.7 \pm 22.2$  and  $1257.0 \pm 131.7$ ; Kruskal-Wallis test,  $p < 0.0001$ ; Dunn's post hoc test, virus injected KO vs any of the other three groups,  $p < 0.0001$ ; Figure 5C). Microglial staining did not show a statistically significant difference between CTRL and KO groups (ratios in CTRL and KO:  $1.89 \pm 0.35$  and  $2.31 \pm 0.35$ , Mann-Whitney test,  $p = 0.45$ ; **Supplementary Figure S4**, panels **A** and **B**). Caspase 3 staining revealed an increase in caspase positive particles in virus injected areas of KO mice (non-injected and virus injected CTRL:  $0.0 \pm 0.0$  and  $46.2 \pm 37.4$ ; non-injected and virus injected KO:  $0.9 \pm 0.9$  and  $151.6 \pm 80.5$ ; Kruskal-Wallis test,  $p < 0.0001$ ; Dunn's post hoc test, virus injected KO vs virus injected CTRL,  $p < 0.05$ ; **Supplementary Figure S4**, panels **A** and **C**), indicating an ongoing apoptosis associated with loss of TDP-43. Together, these results support the idea that TDP-43 depletion causes aberrant neural activity of pyramidal neurons in the PFC that ultimately leads to gliosis and neuron loss.

## Discussion

Our longitudinal *in vivo* calcium imaging studies from awake behaving mice demonstrated aberrant calcium activity in PFC pyramidal neurons prior to neurodegeneration driven by TDP-43 loss-of-function. In particular, we observed that TDP-43 depletion in pyramidal neurons of the PFC triggered an initial hyperactivity followed by a rapid activity decline during disease progression.

## Aberrant neural activity in neurodegeneration

It has long been proposed that excitotoxicity, typically from excessive and prolonged activation of glutamate receptors, is the primary driving force for neurodegenerative disorders such as ALS [55]. Changes in intrinsic excitability which could lead to excitotoxicity, namely hyperexcitability, have been recognized as an early pathological sign in ALS. For instance, cortical hyperexcitability is well documented in transcranial magnetic stimulation (TMS) studies with ALS patients [56, 57]. Hyperexcitability has also been reported in cortical motor neurons of ALS mouse models [58–61]. In addition, multiple lines of motor neurons derived from patient induced pluripotent stem cell (iPSC) harboring mutations in superoxide dismutase 1 (*SOD1*), fused-in-sarcoma (*FUS*), *TDP-43*, or *C9ORF72*, displayed hyperexcitability relative to healthy motor neurons [62, 63].

In contrast, some studies failed to observe hyperexcitability in spinal motor neurons of ALS rodent models, instead reported hypoexcitability in a substantial number of spinal motor neurons before denervation [64]. Again, other iPSC studies reported hypoexcitability displayed by motor neurons derived from patients with *C9ORF72* or *FUS* mutations [65, 66]. Therefore, hypoexcitability has also been proposed as a marker of disease progression in ALS. Moreover, some studies reported transient hyperexcitability followed by a progressive activity loss in iPSC-derived motor neurons from patients with *TDP-43* or *C9ORF72* mutations [67].

Consistent with these previous reports using iPSC models, here we observed biphasic activity changes in neuronal calcium activity triggered by TDP-43 depletion during disease progression from awake behaving mice. In sharp contrast to the relatively stable neuronal calcium activity displayed by CTRL mice, TDP-43 depletion in PFC excitatory neurons leads to an initial hyperactivity followed by a rapid activity decline prior to neuron loss, emphasizing the important role of aberrant neural activity during early stage of the neurodegenerative process. Neuronal hypoactivity following hyperactivity could result from activation of cell intrinsic compensatory mechanism or network compensatory effect from GABAergic inhibition [39]. Dynamic changes in neuronal calcium activity triggered by TDP-43 loss-of-function strongly indicate that disruptive and imbalanced calcium homeostasis might be involved in the initiation and downstream pathways that ultimately lead to neurodegeneration in FTD and ALS.

## **TDP-43 and dysfunctional cytosol calcium in neurodegeneration**

As a ubiquitous second messenger, calcium plays important roles in a variety of cellular processes, from neuronal excitation to synaptic communication. Dysfunctions in cellular calcium homeostasis have been suggested as one of the primary driving forces in neurodegenerative disorders such as AD [68, 69]. Elevated resting intracellular calcium level has been reported in cortical neurons of a transgenic AD mouse model [38]. With two-photon calcium imaging, hyperactive neurons and calcium overloaded neurites were found in proximity of  $\beta$ -amyloid plaques in transgenic AD mouse models [37, 70]. Moreover, it was reported that direct application of soluble  $\beta$ -amyloid was capable of inducing hyperactive calcium activity in even wildtype mice [71].

Interestingly, abnormal intracellular calcium has also been reported in various ALS models carrying TDP-43 mutants. For instance, in motor neurons of a *C. elegans* model, elevated intracellular calcium has been suggested as a driver of mutant TDP-43 mediated neuronal toxicity [72]. Patients-derived motor neurons harboring TDP-43 mutations displayed high glutamate-induced calcium release [73]. In a *Drosophila* model, deficits in motor functions mediated by TDP-43 mutants can be rescued by genetically restoring a voltage-gated calcium channel [74].

Here using *in vivo* calcium imaging from awake behaving mice, we observed dynamic activity changes in PFC pyramidal neurons upon TDP-43 depletion during disease progression. Particularly, TDP-43 depletion triggers initial hyperactivity followed by a rapid decline in calcium activity. Given that TDP-43 plays important roles in RNA splicing, RNA transport and RNA stabilization, TDP-43 depletion might affect

intracellular calcium signaling by directly interfering with intrinsic excitability and/or calcium homeostasis pathways. The possible causes of aberrant calcium activity triggered by loss of TDP-43 could be excessive activation of glutamate receptors, dysregulation in calcium channels, weakening of calcium buffering capacities, or disruptions in mitochondrial and endoplasmic reticulum calcium homeostasis [69]. Follow-up studies will be needed to dissect out major players regarding calcium dysfunctions triggered by TDP-43 depletion.

## Conclusions

TDP-43 depletion in excitatory neurons of the PFC leads to initial hyperactivity followed by a rapid activity decline in excitatory neurons of the PFC, before the ultimate loss of neurons.

## Abbreviations

TDP-43: TAR DNA binding protein 43 kDa, or TARDBP-43

ALS: amyotrophic lateral sclerosis

FTD: frontotemporal dementia

AD: Alzheimer's disease

hnRNPs: heterogeneous nuclear ribonucleoproteins

Miniscope: miniature fluorescence microscope

PFC: prefrontal cortex

ACSF: artificial cerebrospinal fluid

GFAP: glial fibrillary acidic protein

AAV: adeno-associated virus

GRIN lens: gradient index lens

CTRL: control

KO: knockout

AUC: area under curve

TMS: transcranial magnetic stimulation

iPSC: induced pluripotent stem cell

SOD1: superoxide dismutase 1

FUS: fused-in-sarcoma

## Declarations

**Ethical Approval and consent to participate:** Not applicable.

**Consent for publication:** Not applicable.

**Availability of supporting data:** All raw and processed *in vivo* calcium imaging data is available from the corresponding author on reasonable request.

**Competing interests:** The authors declare no competing interests.

**Funding:** This work was initiated at the NIDA IRP and supported by NIH/NIDA/IRP. This work was continued at the University of Wyoming and was further supported by several National Institutes of Health (NIH) grants: 5P20GM121310, R61NS115161, and UG3NS115608.

**Author's contributions:** YL designed and supervised the studies. YL, LZ, YZ, and RT performed brain surgeries including viral injection and GRIN lens implantation. YL, CM, YZ, and RT performed repetitive *in vivo* calcium imaging. BL performed computational analysis of *in vivo* calcium imaging data. RT performed various immunostainings and Nissl staining. RT, GZ, and AJ collected confocal images and slide scanner images. RT and GZ performed data analysis for immunostaining and Nissl staining images. ZZ helped with confocal and slide scanner microscopy setup and data analysis for Nissl staining. CM, RT, and HR performed behavior annotation and verification. PW provided transgenic mouse line. BL, GB, and DTL constructed the miniscope recording system. YL, BL, and RT wrote the manuscript. DTL, ZZ, HR, and PW edited the manuscript. All authors read and approved the final manuscript.

**Acknowledgements:** Not applicable.

**Author's information:**

Bo Liang and Rashmi Thapa contributed equally to this work.

**Affiliations:**

**School of Electrical Engineering & Computer Science, College of Engineering & Mines, University of North Dakota, 243 Centennial Drive Stop 7165, Grand Forks, ND 58202, USA**

Bo Liang

**Department of Zoology and Physiology, University of Wyoming, 1000 E University Avenue, Laramie, WY 82071, USA**

Rashmi Thapa, Amanda Johnston, Hyrum P. Ruby, Zhaojie Zhang, and Yun Li

**Laramie High School, 1710 Boulder Drive, Laramie, WY 82070, USA**

Gracie Zhang

**Intramural Research Program, National Institute on Drug Abuse, National Institutes of Health, 333 Cassell Drive, Baltimore, MD 21224, USA**

Casey Moffitt, Yan Zhang, Giovanni Barbera, and Da-Ting Lin

**Department of Pathology, Johns Hopkins University School of Medicine, 725 N. Wolfe Street, Baltimore, MD 21205, USA**

Philip C. Wong

**The Solomon H. Snyder Department of Neuroscience, Johns Hopkins University School of Medicine, 725 N. Wolfe Street, Baltimore, MD 21205, USA**

Philip C. Wong and Da-Ting Lin

## References

1. Polymenidou M, Lagier-Tourenne C, Hutt KR, Huelga SC, Moran J, Liang TY, Ling SC, Sun E, Wancewicz E, Mazur C, et al. Long pre-mRNA depletion and RNA missplicing contribute to neuronal vulnerability from loss of TDP-43. *Nat Neurosci.* 2011;14(4):459–68.
2. Tollervey JR, Curk T, Rogelj B, Briese M, Cereda M, Kayikci M, Konig J, Hortobagyi T, Nishimura AL, Zupunski V, et al. Characterizing the RNA targets and position-dependent splicing regulation by TDP-43. *Nat Neurosci.* 2011;14(4):452–8.
3. Amador-Ortiz C, Lin WL, Ahmed Z, Personett D, Davies P, Duara R, Graff-Radford NR, Hutton ML, Dickson DW. TDP-43 immunoreactivity in hippocampal sclerosis and Alzheimer's disease. *Ann Neurol.* 2007;61(5):435–45.
4. Janssens J, Van Broeckhoven C. Pathological mechanisms underlying TDP-43 driven neurodegeneration in FTLD-ALS spectrum disorders. *Hum Mol Genet.* 2013;22(R1):R77–87.
5. Neumann M, Sampathu DM, Kwong LK, Truax AC, Micsenyi MC, Chou TT, Bruce J, Schuck T, Grossman M, Clark CM, et al. Ubiquitinated TDP-43 in frontotemporal lobar degeneration and amyotrophic lateral sclerosis. *Science.* 2006;314(5796):130–3.
6. Ling SC, Polymenidou M, Cleveland DW. Converging mechanisms in ALS and FTD: disrupted RNA and protein homeostasis. *Neuron.* 2013;79(3):416–38.
7. Kabashi E, Valdmanis PN, Dion P, Spiegelman D, McConkey BJ, Vande Velde C, Bouchard JP, Lacomblez L, Pochigaeva K, Salachas F, et al. TARDBP mutations in individuals with sporadic and familial amyotrophic lateral sclerosis. *Nat Genet.* 2008;40(5):572–4.

8. Sreedharan J, Blair IP, Tripathi VB, Hu X, Vance C, Rogelj B, Ackerley S, Durnall JC, Williams KL, Buratti E, et al. TDP-43 mutations in familial and sporadic amyotrophic lateral sclerosis. *Science*. 2008;319(5870):1668–72.
9. Borroni B, Bonvicini C, Alberici A, Buratti E, Agosti C, Archetti S, Papetti A, Stuani C, Di Luca M, Gennarelli M, et al. Mutation within TARDBP leads to frontotemporal dementia without motor neuron disease. *Hum Mutat*. 2009;30(11):E974–83.
10. Kovacs GG, Murrell JR, Horvath S, Haraszti L, Majtenyi K, Molnar MJ, Budka H, Ghetti B, Spina S. TARDBP variation associated with frontotemporal dementia, supranuclear gaze palsy, and chorea. *Mov Disord*. 2009;24(12):1843–7.
11. Buratti E, Brindisi A, Giombi M, Tisminetzky S, Ayala YM, Baralle FE. TDP-43 binds heterogeneous nuclear ribonucleoprotein A/B through its C-terminal tail: an important region for the inhibition of cystic fibrosis transmembrane conductance regulator exon 9 splicing. *J Biol Chem*. 2005;280(45):37572–84.
12. Lee EB, Lee VM, Trojanowski JQ. Gains or losses: molecular mechanisms of TDP43-mediated neurodegeneration. *Nat Rev Neurosci*. 2011;13(1):38–50.
13. Ritson GP, Custer SK, Freibaum BD, Guinto JB, Geffel D, Moore J, Tang W, Winton MJ, Neumann M, Trojanowski JQ, et al. TDP-43 mediates degeneration in a novel *Drosophila* model of disease caused by mutations in VCP/p97. *J Neurosci*. 2010;30(22):7729–39.
14. Vanden Broeck L, Callaerts P, Dermaut B. TDP-43-mediated neurodegeneration: towards a loss-of-function hypothesis? *Trends Mol Med*. 2014;20(2):66–71.
15. Chiang PM, Ling J, Jeong YH, Price DL, Aja SM, Wong PC. Deletion of TDP-43 down-regulates *Tbc1d1*, a gene linked to obesity, and alters body fat metabolism. *Proc Natl Acad Sci U S A*. 2010;107(37):16320–4.
16. Donde A, Sun M, Ling JP, Braunstein KE, Pang B, Wen X, Cheng X, Chen L, Wong PC. Splicing repression is a major function of TDP-43 in motor neurons. *Acta Neuropathol*. 2019;138(5):813–26.
17. Feiguin F, Godena VK, Romano G, D'Ambrogio A, Klima R, Baralle FE. Depletion of TDP-43 affects *Drosophila* motoneurons terminal synapsis and locomotive behavior. *FEBS Lett*. 2009;583(10):1586–92.
18. Iguchi Y, Katsuno M, Niwa J, Takagi S, Ishigaki S, Ikenaka K, Kawai K, Watanabe H, Yamanaka K, Takahashi R, et al. Loss of TDP-43 causes age-dependent progressive motor neuron degeneration. *Brain*. 2013;136(Pt 5):1371–82.
19. Kraemer BC, Schuck T, Wheeler JM, Robinson LC, Trojanowski JQ, Lee VM, Schellenberg GD. Loss of murine TDP-43 disrupts motor function and plays an essential role in embryogenesis. *Acta Neuropathol*. 2010;119(4):409–19.
20. Schmid B, Hruscha A, Hogl S, Banzhaf-Strathmann J, Strecker K, van der Zee J, Teucke M, Eimer S, Hegemann J, Kittelmann M, et al. Loss of ALS-associated TDP-43 in zebrafish causes muscle degeneration, vascular dysfunction, and reduced motor neuron axon outgrowth. *Proc Natl Acad Sci U S A*. 2013;110(13):4986–91.

21. Zhang T, Hwang HY, Hao H, Talbot C Jr, Wang J. *Caenorhabditis elegans* RNA-processing protein TDP-1 regulates protein homeostasis and life span. *J Biol Chem.* 2012;287(11):8371–82.
22. Diaper DC, Adachi Y, Sutcliffe B, Humphrey DM, Elliott CJ, Stepto A, Ludlow ZN, Vanden Broeck L, Callaerts P, Dermaut B, et al. Loss and gain of *Drosophila* TDP-43 impair synaptic efficacy and motor control leading to age-related neurodegeneration by loss-of-function phenotypes. *Hum Mol Genet.* 2013;22(8):1539–57.
23. Vanden Broeck L, Naval-Sanchez M, Adachi Y, Diaper D, Dourlen P, Chapuis J, Kleinberger G, Gistelinc M, Van Broeckhoven C, Lambert JC, et al. TDP-43 loss-of-function causes neuronal loss due to defective steroid receptor-mediated gene program switching in *Drosophila*. *Cell Rep.* 2013;3(1):160–72.
24. Stallings NR, Puttapparthi K, Luther CM, Burns DK, Elliott JL. Progressive motor weakness in transgenic mice expressing human TDP-43. *Neurobiol Dis.* 2010;40(2):404–14.
25. Wegorzewska I, Bell S, Cairns NJ, Miller TM, Baloh RH. TDP-43 mutant transgenic mice develop features of ALS and frontotemporal lobar degeneration. *Proc Natl Acad Sci U S A.* 2009;106(44):18809–14.
26. Wils H, Kleinberger G, Janssens J, Pereson S, Joris G, Cuijt I, Smits V, Ceuterick-de Groote C, Van Broeckhoven C, Kumar-Singh S. TDP-43 transgenic mice develop spastic paralysis and neuronal inclusions characteristic of ALS and frontotemporal lobar degeneration. *Proc Natl Acad Sci U S A.* 2010;107(8):3858–63.
27. Igaz LM, Kwong LK, Lee EB, Chen-Plotkin A, Swanson E, Unger T, Malunda J, Xu Y, Winton MJ, Trojanowski JQ, et al. Dysregulation of the ALS-associated gene TDP-43 leads to neuronal death and degeneration in mice. *J Clin Invest.* 2011;121(2):726–38.
28. Nana AL, Sidhu M, Gaus SE, Hwang JL, Li L, Park Y, Kim EJ, Pasquini L, Allen IE, Rankin KP, et al. Neurons selectively targeted in frontotemporal dementia reveal early stage TDP-43 pathobiology. *Acta Neuropathol.* 2019;137(1):27–46.
29. Vatsavayai SC, Yoon SJ, Gardner RC, Gendron TF, Vargas JN, Trujillo A, Pribadi M, Phillips JJ, Gaus SE, Hixson JD, et al. Timing and significance of pathological features in C9orf72 expansion-associated frontotemporal dementia. *Brain.* 2016;139(Pt 12):3202–16.
30. Ling JP, Pletnikova O, Troncoso JC, Wong PC. TDP-43 repression of nonconserved cryptic exons is compromised in ALS-FTD. *Science.* 2015;349(6248):650–5.
31. Sun M, Bell W, LaClair KD, Ling JP, Han H, Kageyama Y, Pletnikova O, Troncoso JC, Wong PC, Chen LL. Cryptic exon incorporation occurs in Alzheimer's brain lacking TDP-43 inclusion but exhibiting nuclear clearance of TDP-43. *Acta Neuropathol.* 2017;133(6):923–31.
32. Klim JR, Williams LA, Limone F, Guerra San Juan I, Davis-Dusenbery BN, Mordes DA, Burberry A, Steinbaugh MJ, Gamage KK, Kirchner R, et al. ALS-implicated protein TDP-43 sustains levels of STMN2, a mediator of motor neuron growth and repair. *Nat Neurosci.* 2019;22(2):167–79.
33. Melamed Z, Lopez-Erauskin J, Baughn MW, Zhang O, Drenner K, Sun Y, Freyermuth F, McMahon MA, Beccari MS, Artates JW, et al. Premature polyadenylation-mediated loss of stathmin-2 is a hallmark

- of TDP-43-dependent neurodegeneration. *Nat Neurosci*. 2019;22(2):180–90.
34. Brown A-L, Wilkins OG, Keuss MJ, Hill SE, Zanovello M, Lee WC, Lee FCY, Masino L, Qi YA, Bryce-Smith S, et al: **Common ALS/FTD risk variants in UNC13A exacerbate its cryptic splicing and loss upon TDP-43 mislocalization.** *bioRxiv* 2021.
35. Ma XR, Prudencio M, Koike Y, Vatsavayai SC, Kim G, Harbinski F, Rodriguez CM, Schmidt HB, Cummings BB, Wyatt DW, et al: **TDP-43 represses cryptic exon inclusion in FTD/ALS gene UNC13A.** *bioRxiv* 2021.
36. Anekonda TS, Quinn JF. Calcium channel blocking as a therapeutic strategy for Alzheimer's disease: the case for isradipine. *Biochim Biophys Acta*. 2011;1812(12):1584–90.
37. Busche MA, Eichhoff G, Adelsberger H, Abramowski D, Wiederhold KH, Haass C, Staufenbiel M, Konnerth A, Garaschuk O. Clusters of hyperactive neurons near amyloid plaques in a mouse model of Alzheimer's disease. *Science*. 2008;321(5896):1686–9.
38. Lopez JR, Lyckman A, Oddo S, Laferla FM, Querfurth HW, Shtifman A. Increased intraneuronal resting [Ca<sup>2+</sup>] in adult Alzheimer's disease mice. *J Neurochem*. 2008;105(1):262–71.
39. Palop JJ, Chin J, Roberson ED, Wang J, Thwin MT, Bien-Ly N, Yoo J, Ho KO, Yu GQ, Kreitzer A, et al. Aberrant excitatory neuronal activity and compensatory remodeling of inhibitory hippocampal circuits in mouse models of Alzheimer's disease. *Neuron*. 2007;55(5):697–711.
40. Styr B, Slutsky I. Imbalance between firing homeostasis and synaptic plasticity drives early-phase Alzheimer's disease. *Nat Neurosci*. 2018;21(4):463–73.
41. Zhang W, Zhang L, Liang B, Schroeder D, Zhang ZW, Cox GA, Li Y, Lin DT. Hyperactive somatostatin interneurons contribute to excitotoxicity in neurodegenerative disorders. *Nat Neurosci*. 2016;19(4):557–9.
42. Sephton CF, Good SK, Atkin S, Dewey CM, Mayer P 3rd, Herz J, Yu G. TDP-43 is a developmentally regulated protein essential for early embryonic development. *J Biol Chem*. 2010;285(9):6826–34.
43. Wu LS, Cheng WC, Hou SC, Yan YT, Jiang ST, Shen CK. TDP-43, a neuro-pathosignature factor, is essential for early mouse embryogenesis. *Genesis*. 2010;48(1):56–62.
44. Thapa R, Liang B, Liu R, Li Y. **Stereotaxic Viral Injection and Gradient-Index Lens Implantation for Deep Brain In Vivo Calcium Imaging.** *J Vis Exp* 2021(176).
45. Zhang L, Liang B, Barbera G, Hawes S, Zhang Y, Stump K, Baum I, Yang Y, Li Y, Lin DT. Miniscope GRIN Lens System for Calcium Imaging of Neuronal Activity from Deep Brain Structures in Behaving Animals. *Curr Protoc Neurosci*. 2019;86(1):e56.
46. Liang B, Zhang L, Moffitt C, Li Y, Lin DT. An open-source automated surgical instrument for microendoscope implantation. *J Neurosci Methods*. 2019;311:83–8.
47. Barbera G, Liang B, Zhang L, Gerfen CR, Culurciello E, Chen R, Li Y, Lin DT. Spatially Compact Neural Clusters in the Dorsal Striatum Encode Locomotion Relevant Information. *Neuron*. 2016;92(1):202–13.

48. Liang B, Zhang L, Barbera G, Fang W, Zhang J, Chen X, Chen R, Li Y, Lin DT. Distinct and Dynamic ON and OFF Neural Ensembles in the Prefrontal Cortex Code Social Exploration. *Neuron*. 2018;100(3):700–14 e709.
49. Zhang Y, Denman AJ, Liang B, Werner CT, Beacher NJ, Chen R, Li Y, Shaham Y, Barbera G, Lin DT: **Detailed mapping of behavior reveals the formation of prelimbic neural ensembles across operant learning.** *Neuron* 2021.
50. Pnevmatikakis EA, Giovannucci A. NoRMCorre: An online algorithm for piecewise rigid motion correction of calcium imaging data. *J Neurosci Methods*. 2017;291:83–94.
51. Giovannucci A, Friedrich J, Gunn P, Kalfon J, Brown BL, Koay SA, Taxidis J, Najafi F, Gauthier JL, Zhou P, et al: **CalmAn an open source tool for scalable calcium imaging data analysis.** *Elife* 2019, **8**.
52. Pnevmatikakis EA, Soudry D, Gao Y, Machado TA, Merel J, Pfau D, Reardon T, Mu Y, Lacefield C, Yang W, et al. Simultaneous Denoising, Deconvolution, and Demixing of Calcium Imaging Data. *Neuron*. 2016;89(2):285–99.
53. Zhou P, Resendez SL, Rodriguez-Romaguera J, Jimenez JC, Neufeld SQ, Giovannucci A, Friedrich J, Pnevmatikakis EA, Stuber GD, Hen R. Efficient and accurate extraction of in vivo calcium signals from microendoscopic video data. *Elife*. 2018;7:e28728.
54. Sherwood CC, Stimpson CD, Raghanti MA, Wildman DE, Uddin M, Grossman LI, Goodman M, Redmond JC, Bonar CJ, Erwin JM, et al. Evolution of increased glia-neuron ratios in the human frontal cortex. *Proc Natl Acad Sci U S A*. 2006;103(37):13606–11.
55. King AE, Woodhouse A, Kirkcaldie MT, Vickers JC. Excitotoxicity in ALS: Overstimulation, or overreaction? *Exp Neurol*. 2016;275 Pt 1:162–71.
56. Vucic S, Kiernan MC. Utility of transcranial magnetic stimulation in delineating amyotrophic lateral sclerosis pathophysiology. *Handb Clin Neurol*. 2013;116:561–75.
57. Williams KL, Fifita JA, Vucic S, Durnall JC, Kiernan MC, Blair IP, Nicholson GA. Pathophysiological insights into ALS with C9ORF72 expansions. *J Neurol Neurosurg Psychiatry*. 2013;84(8):931–5.
58. Kim J, Hughes EG, Shetty AS, Arlotta P, Goff LA, Bergles DE, Brown SP. Changes in the Excitability of Neocortical Neurons in a Mouse Model of Amyotrophic Lateral Sclerosis Are Not Specific to Corticospinal Neurons and Are Modulated by Advancing Disease. *J Neurosci*. 2017;37(37):9037–53.
59. Pieri M, Albo F, Gaetti C, Spalloni A, Bengtson CP, Longone P, Cavalcanti S, Zona C. Altered excitability of motor neurons in a transgenic mouse model of familial amyotrophic lateral sclerosis. *Neurosci Lett*. 2003;351(3):153–6.
60. Pieri M, Carunchio I, Curcio L, Mercuri NB, Zona C. Increased persistent sodium current determines cortical hyperexcitability in a genetic model of amyotrophic lateral sclerosis. *Exp Neurol*. 2009;215(2):368–79.
61. Saba L, Viscomi MT, Caioli S, Pignataro A, Bisicchia E, Pieri M, Molinari M, Ammassari-Teule M, Zona C. Altered Functionality, Morphology, and Vesicular Glutamate Transporter Expression of Cortical Motor Neurons from a Presymptomatic Mouse Model of Amyotrophic Lateral Sclerosis. *Cereb Cortex*. 2016;26(4):1512–28.

62. Huang X, Roet KCD, Zhang L, Brault A, Berg AP, Jefferson AB, Klug-McLeod J, Leach KL, Vincent F, Yang H, et al. Human amyotrophic lateral sclerosis excitability phenotype screen: Target discovery and validation. *Cell Rep.* 2021;35(10):109224.
63. Wainger BJ, Kiskinis E, Mellin C, Wiskow O, Han SS, Sandoe J, Perez NP, Williams LA, Lee S, Boulting G, et al. Intrinsic membrane hyperexcitability of amyotrophic lateral sclerosis patient-derived motor neurons. *Cell Rep.* 2014;7(1):1–11.
64. Delestree N, Manuel M, Iglesias C, Elbasiouny SM, Heckman CJ, Zytnicki D. Adult spinal motoneurons are not hyperexcitable in a mouse model of inherited amyotrophic lateral sclerosis. *J Physiol.* 2014;592(7):1687–703.
65. Guo W, Naujock M, Fumagalli L, Vandoorne T, Baatsen P, Boon R, Ordovas L, Patel A, Welters M, Vanwelden T, et al. HDAC6 inhibition reverses axonal transport defects in motor neurons derived from FUS-ALS patients. *Nat Commun.* 2017;8(1):861.
66. Sareen D, O'Rourke JG, Meera P, Muhammad AK, Grant S, Simpkinson M, Bell S, Carmona S, Ornelas L, Sahabian A, et al. Targeting RNA foci in iPSC-derived motor neurons from ALS patients with a C9ORF72 repeat expansion. *Sci Transl Med.* 2013;5(208):208ra149.
67. Devlin AC, Burr K, Borooah S, Foster JD, Cleary EM, Geti I, Vallier L, Shaw CE, Chandran S, Miles GB. Human iPSC-derived motoneurons harbouring TARDBP or C9ORF72 ALS mutations are dysfunctional despite maintaining viability. *Nat Commun.* 2015;6:5999.
68. Magi S, Castaldo P, Macri ML, Maiolino M, Matteucci A, Bastioli G, Gratteri S, Amoroso S, Lariccia V. Intracellular Calcium Dysregulation: Implications for Alzheimer's Disease. *Biomed Res Int.* 2016;2016:6701324.
69. Marambaud P, Dreses-Werringloer U, Vingtdeux V. Calcium signaling in neurodegeneration. *Mol Neurodegener.* 2009;4:20.
70. Kuchibhotla KV, Goldman ST, Lattarulo CR, Wu HY, Hyman BT, Bacskai BJ. Abeta plaques lead to aberrant regulation of calcium homeostasis in vivo resulting in structural and functional disruption of neuronal networks. *Neuron.* 2008;59(2):214–25.
71. Busche MA, Chen X, Henning HA, Reichwald J, Staufenbiel M, Sakmann B, Konnerth A. Critical role of soluble amyloid-beta for early hippocampal hyperactivity in a mouse model of Alzheimer's disease. *Proc Natl Acad Sci U S A.* 2012;109(22):8740–5.
72. Aggad D, Veriepe J, Tauffenberger A, Parker JA. TDP-43 toxicity proceeds via calcium dysregulation and necrosis in aging *Caenorhabditis elegans* motor neurons. *J Neurosci.* 2014;34(36):12093–103.
73. Dafinca R, Barbagallo P, Farrimond L, Candalija A, Scaber J, Ababneh NA, Sathyaprakash C, Vowles J, Cowley SA, Talbot K. Impairment of Mitochondrial Calcium Buffering Links Mutations in C9ORF72 and TARDBP in iPS-Derived Motor Neurons from Patients with ALS/FTD. *Stem Cell Reports.* 2020;14(5):892–908.
74. Lembke KM, Morton DB. Exploring the Interaction of *Drosophila* TDP-43 and the Type II Voltage-Gated Calcium Channel, *Cacophony*, in Regulating Motor Function and Behavior. *J Exp Neurosci.* 2017;11:1179069517740892.

# Figures

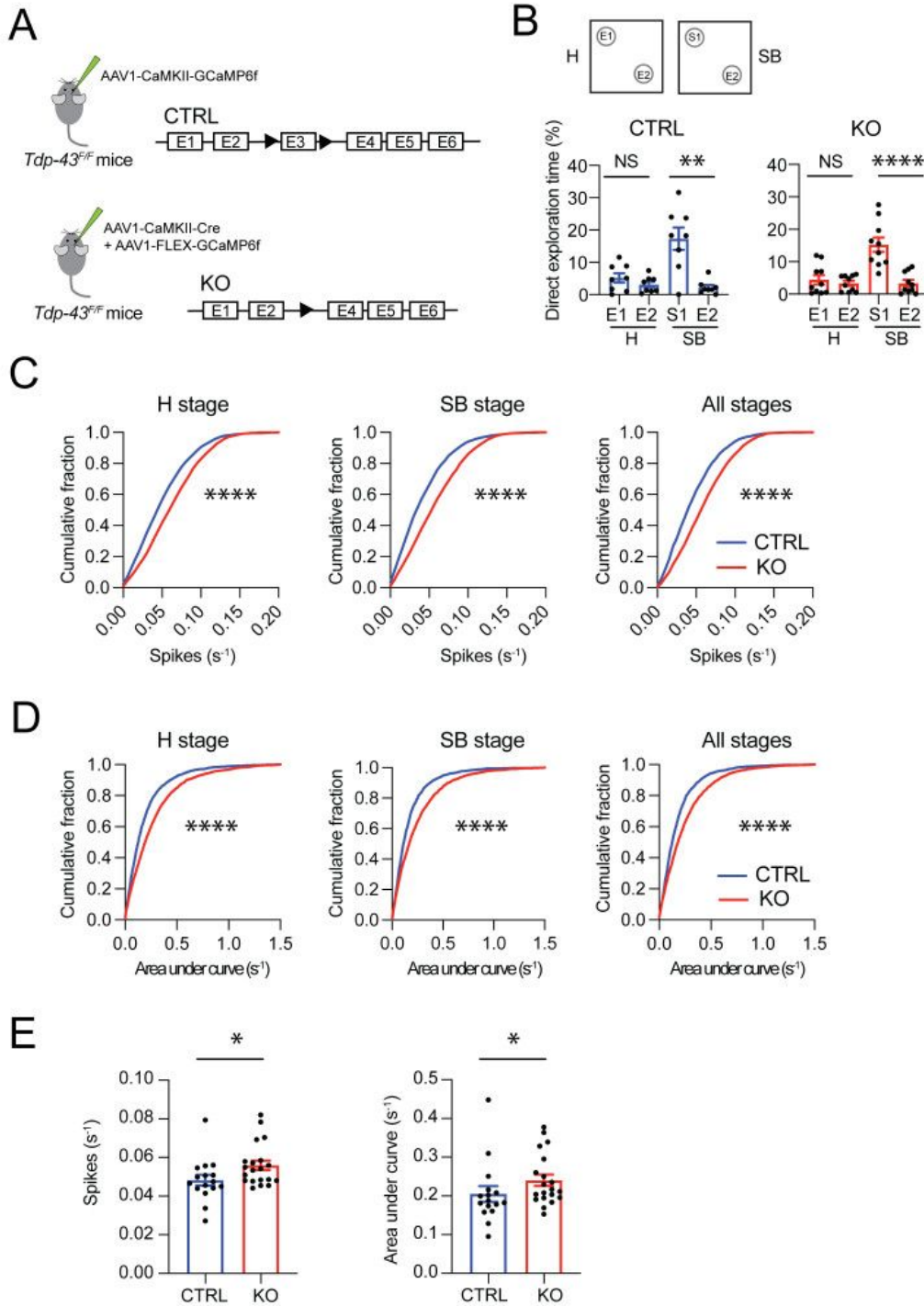


Figure 1

Short-term TDP-43 depletion elicits hyperactivity in neuronal calcium activity in the PFC.

**A.** Strategy for generating CTRL and KO mice and labelling excitatory neurons in the PFC of *Tdp-43<sup>F/F</sup>* mice with a genetically encoded fluorescent calcium indicator, GCaMP6f. CTRL mice were injected with AAV1-CaMKII-GCaMP6f virus to label excitatory neurons with GCaMP6f. KO mice were injected with a viral mix containing AAV1-CaMKII-Cre virus and a Cre-dependent virus, AAV1-CAG-Flex-GCaMP6f, to label TDP-43 depleted excitatory neurons with GCaMP6f.

**B.** Top: schematic paradigm for social behavior test composed of two 10-minutes stages, habituation (H) and sociability (SB) stages. E1 and E2 represent empty containers; S1 represents stranger 1, a never-before-met same sex social target. Bottom: Bar graphs showing the time percentages mice spent during H and SB stages, for direct exploration of E1, E2, and S1, from CTRL (n = 8 mice) and KO (n = 10 mice) groups (Mann-Whitney test).

**C** and **D.** Cumulative probability distribution panels depicting significant shifts towards higher spike frequency (**C**) and area under curve (**D**) in neuronal calcium traces from KO mice compared to CTRL mice, during H and SB stages separately, as well as, during both stages combined. CTRL and KO at H stage: n = 2355 and n = 2828 neurons; CTRL and KO at SB stage: n = 2364 and n = 2842 neurons; CTRL and KO at combined stages: n = 2414 and n = 2930 neurons; Kolmogorov-Smirnov test.

**E.** Bar graphs showing comparisons of the averaged spike frequency (left panel) and area under curve (right panel) in neuronal calcium traces from the H and SB stages of individual CTRL and KO mice (CTRL: n = 16 stages from 8 mice; KO: n = 20 stages from 10 mice; Mann-Whitney test). Bar graphs represent mean  $\pm$  SEM. NS, not significant; \*, p < 0.05; \*\*, p < 0.01; \*\*\*\*, p < 0.0001.

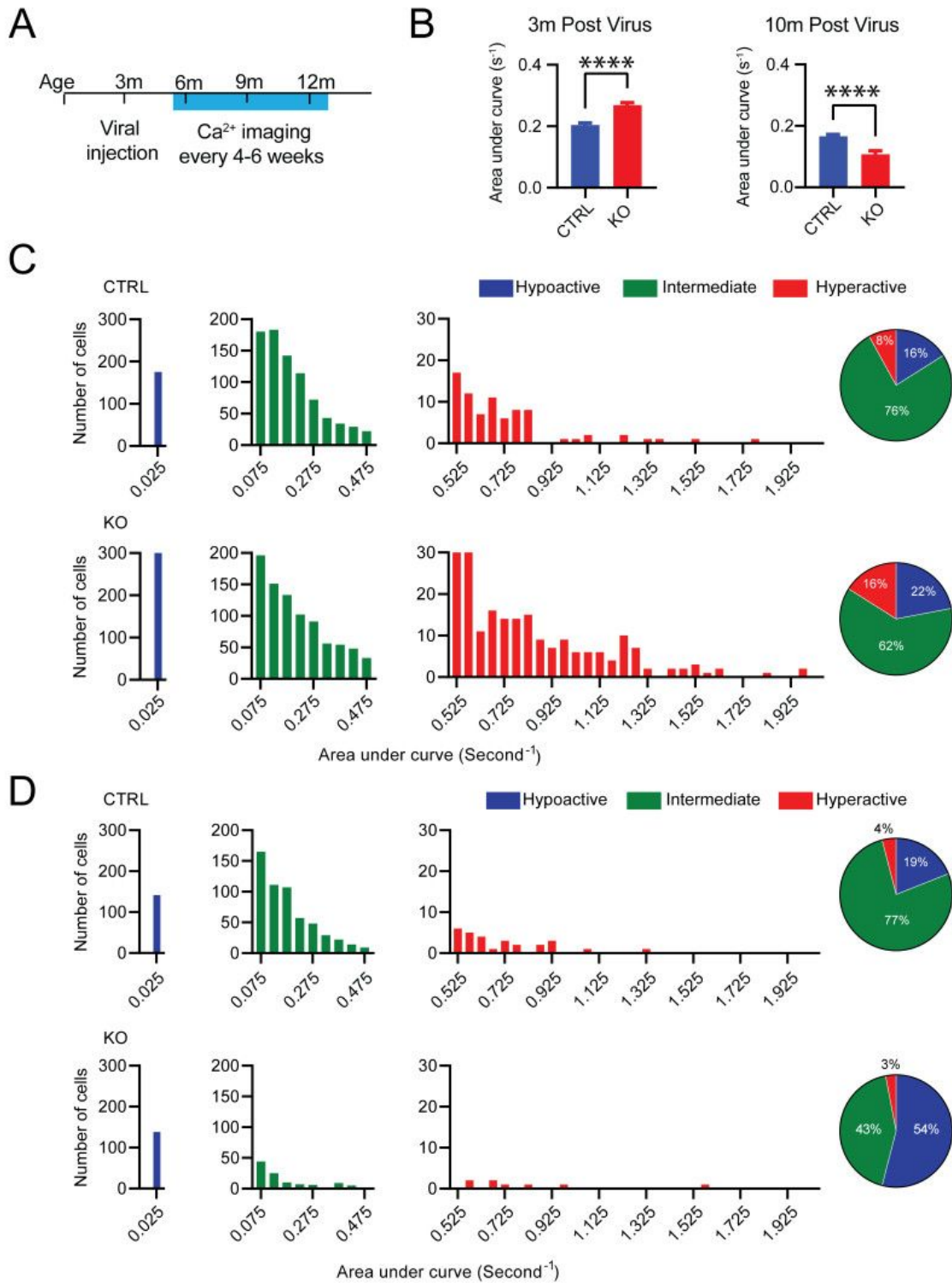


**Figure 2**

Repetitive *in vivo* calcium imaging reveals dynamic changes in neuronal calcium activity following TDP-43 depletion.

A. Schematic diagram showing the experimental timeline.

**B.** Bar graphs represent the averaged area under curve values of neuronal calcium traces during the H stage from CTRL and KO mice. Left panel reveals neuronal hyperactivity in KO mice compared to CTRL mice at 3 months post viral injection (n = 1074 and n = 1400 neurons from 4 CTRL mice and 4 KO mice; Kolmogorov-Smirnov test). Right panel reveals neuronal hypoactivity in KO mice compared to CTRL mice at 10 months post viral injection (n = 731 and n = 256 neurons from 4 CTRL mice and 4 KO mice; Kolmogorov-Smirnov test).

**C.** Histograms illustrating the distribution of area under curve values in calcium traces during the H stage from CTRL group (top, n = 1074 neurons from 4 mice) and KO group (bottom, n = 1400 neurons from 4 mice) at 3 months post viral injection. Pie charts showing the relative proportion of hypoactive, intermediate and hyperactive neurons.

**D.** Histograms illustrating the distribution of area under curve values in calcium traces during the H stage from CTRL group (top, n = 731 neurons from 4 mice) and KO group (bottom, n = 256 neurons from 4 mice) at 10 months post viral injection. Pie charts showing the relative proportion of hypoactive, intermediate and hyperactive neurons. Bar graphs represent mean  $\pm$  SEM. \*\*\*\*,  $p < 0.0001$ .

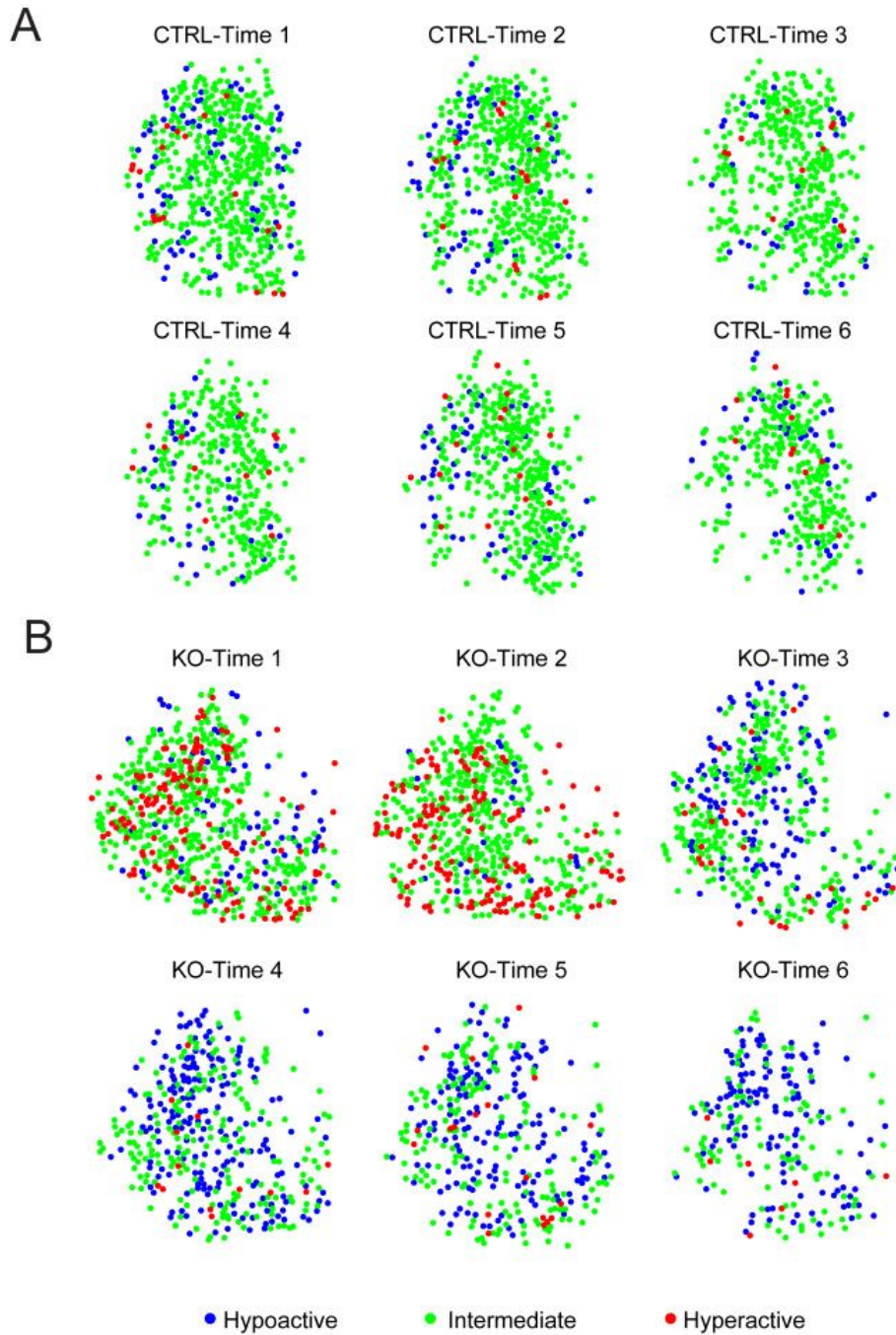


**Figure 3**

**Representative cell activity maps across time.**

Cell activity maps of a representative CTRL mouse (**A**) and KO mouse (**B**) at six different time points (30 - 45 days apart) following viral injection. Dots in cell activity maps represent individual neurons. Colors indicate hypoactive (blue), intermediate (green), and hyperactive (red) neurons, according to the area

under curve values in calcium traces during the H stage applied with similar thresholds as that of Figure 2. CTRL cell activity maps display relatively stable proportions of neuronal activity over time. By contrast, KO cell activity maps reveal large numbers of hyperactive cells at earlier time points while hypoactive cells at later time points.

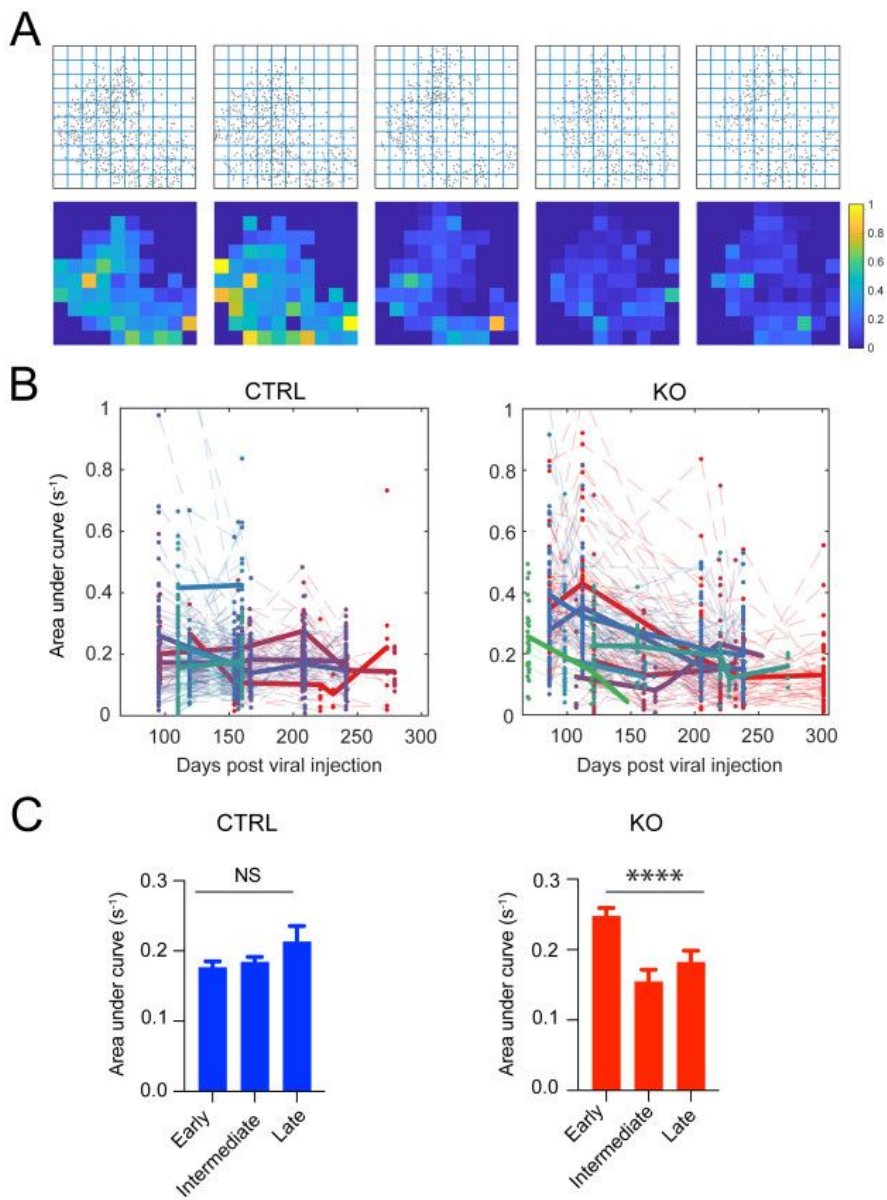


## Figure 4

### Rapid activity declines associated with long term TDP-43 depletion

- A.** Diagrams from a representative KO mouse showing the divided multiple small sub-areas (each with a size of 65 mm by 65 mm, top) and the regional area under curve (AUC) values averaged from neurons within the same sub-areas at different time points (bottom).
- B.** Plots showing dynamic activity changes over time in regional AUC values averaged from neurons within the same divided sub-areas of CTRL and KO mice. Each dot represents AUC value from one small sub-area. Dashed lines indicate dynamic activity changes from individual small sub-areas. Solid lines are the averaged AUC activity changes from individual mice. Different colors representing different mice.
- C.** Bar graphs are quantifications of the averaged AUC values measured from all small sub-areas at three time periods: early (80-100 days post viral injection), intermediate (150-200 days post viral injection), and late (250-300 days post viral injection) stages. AUC values were measured only from small sub-areas containing more than 3 active neurons. CTRL at early, intermediate, and late stages:  $n = 175$ ,  $n = 254$  and  $n = 70$  small sub-areas from 8 mice; KO at early, intermediate, and late stages:  $n = 285$ ,  $n = 69$  and  $n = 48$  small sub-areas from 10 mice. Kruskal-Wallis test and Dunn's post hoc test. Bar graphs represent mean  $\pm$  SEM. NS, not significant; \*\*\*\*,  $p < 0.0001$ .

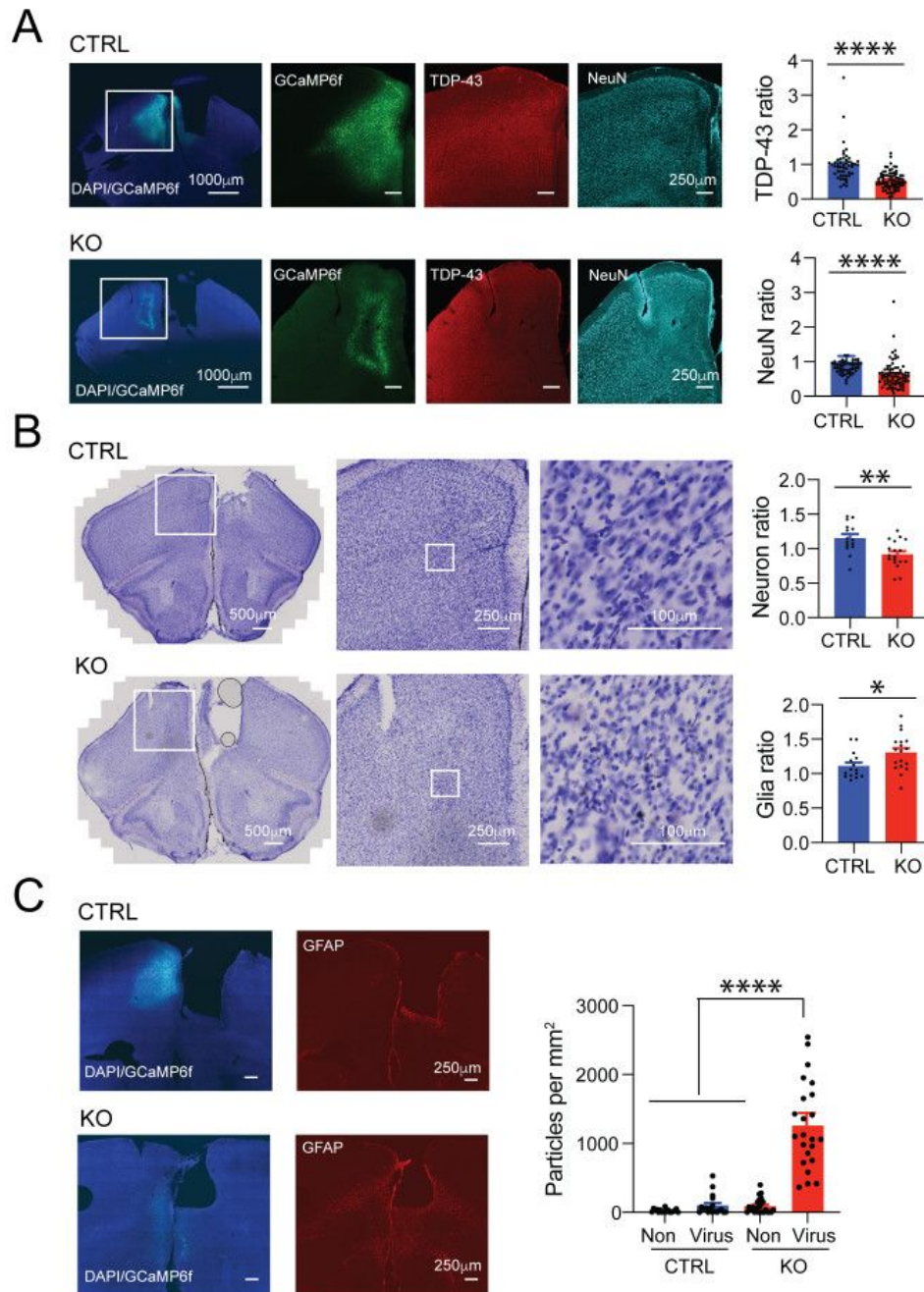


**Figure 5**

**Gliosis and neuron loss in TDP-43 deficient areas of the PFC**

**A.** Representative immunofluorescence images for TDP-43 and NeuN from a CTRL mouse (top) and a KO mouse (bottom). Images from left to right: DAPI stained whole brain sections (merged green and blue channels, scale bars, 1000 mm); high magnification images of the enclosed area for GCaMP6f (green

channel), TDP-43 (red channel), and NeuN (cyan channel). Scale bars, 250  $\mu$ m. Bar graphs showing quantifications of TDP-43 (top) and NeuN (bottom) from brain sections of CTRL and KO groups. The ratios of positively stained particle densities between the virus injected and non-injected areas were compared between CTRL and KO groups (CTRL and KO: n = 49 and n = 75 brain sections, Mann-Whitney test).

**B.** Representative Nissl staining images from a CTRL mouse (top) and a KO mouse (bottom). Images from left to right are cresyl violet stained whole brain sections, enlarged PFC regions and high magnification of enclosed areas. Scale bars, 250  $\mu$ m. Bar graphs showing quantifications of neuronal (top) and glial (bottom) particles in KO mice compared to CTRL mice. The ratios of particle densities between the virus injected and non-injected areas were compared between CTRL and KO groups (CTRL and KO: n = 15 and n = 18 brain sections, Mann-Whitney test).

**C.** Representative immunofluorescence images for GFAP from a CTRL mouse (top) and a KO mouse (bottom). Images showing DAPI stained PFC regions (left, merged green and blue channels) and GFAP immunostaining (right, red channel). Scale bars, 250  $\mu$ m. Bar graph showing quantification of GFAP positive particle densities of virus injected and non-injected areas from CTRL and KO groups (CTRL and KO: n = 18 and n = 24 brain sections; Kruskal-Wallis test and Dunn's post hoc test). Bar graphs represent mean  $\pm$  SEM. \*, p < 0.05; \*\*, p < 0.01; \*\*\*\*, p < 0.0001.

## Supplementary Files

This is a list of supplementary files associated with this preprint. Click to download.

- [FigureS1.pdf](#)
- [FigureS2.pdf](#)
- [FigureS3.pdf](#)
- [FigureS4.pdf](#)